

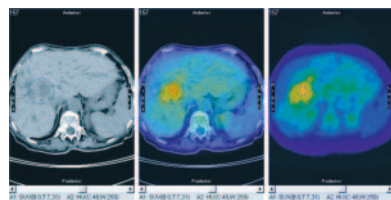
THIS MONTH IN JNM

Mazzaferri reviews the basis for current management of differentiated thyroid carcinoma and looks at the debate over treatment of patients with high serum thyroglobulin levels but negative whole-body ^{131}I scans. **Page 1079**

Mabuchi and colleagues measure ^{131}I -MIBG uptake to assess changes in cardiac sympathetic nerves during follow-up after the Maze cardiac procedure in patients with mitral valve disease and correlate these changes with left ventricular function. **Page 1089**

Chow and colleagues evaluate the prognostic significance of dipyridamole-induced ischemic electrocardiograph changes in patients with normal ^{82}Rb PET myocardial perfusion images. **Page 1095**

Akincioglu and colleagues assess the feasibility of diastolic function evaluation using standard 16-frame postexercise gated $^{99\text{m}}\text{Tc}$ -sestamibi myocardial perfusion SPECT and determine the relationship of key variables in patients with normal myocardial perfusion to derive and validate normal limits. **Page 1102**

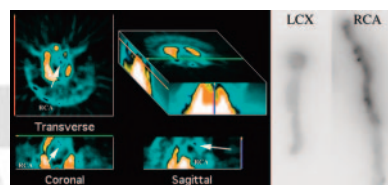


Koch and colleagues report on an automated method developed for standardized quantification of ^{123}I -FP-CIT SPECT and discuss its potential in facilitating objective intra- and interindividual comparisons as well as multicenter trials. . **Page 1109**

Pinborg and colleagues describe a bolus/infusion approach to accurate and pre-

cise quantification of ^{123}I -PE2I, a novel tracer that binds to brain dopamine transporters, and report on its pharmacokinetics in a 5-person trial. **Page 1119**

Giovacchini and colleagues detail studies indicating the critical importance of partial-volume correction in PET receptor studies of patients with temporal lobe epilepsy that is refractory to medical therapy. **Page 1128**



Ng and colleagues evaluate ^{18}F -FDG PET and hybrid CT/MRI and their visual correlation for the identification of primary tumors and cervical nodal metastases of squamous cell carcinoma of the oral cavity and compare these results with findings at surgery. **Page 1136**

Schwarz and colleagues describe the use of sequential ^{18}F -FDG PET to predict response after the first and second cycles of standardized chemotherapy for metastatic breast cancer and report on the potential for this technique in individualizing treatment approaches. **Page 1144**

Hemm and colleagues assess the clinical feasibility of integration of stereotactic SPECT with ^{201}Tl in stereotactic MRI-based planning of brain tumor biopsy and document the prognostic value of this technique. **Page 1151**

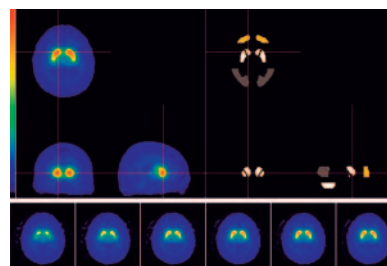
Reinhardt and colleagues provide a preliminary report on the effectiveness of ^{18}F -FDG PET/CT in the detection of perihilar cholangiocarcinoma in extrahepatic bile duct strictures. **Page 1158**

Ma and colleagues review current medical literature on the management of patients with differentiated thyroid carcinoma who have positive thyroglobulin tests but negative ^{131}I whole-body scans to evaluate the efficacy of ^{131}I treatment. **Page 1164**

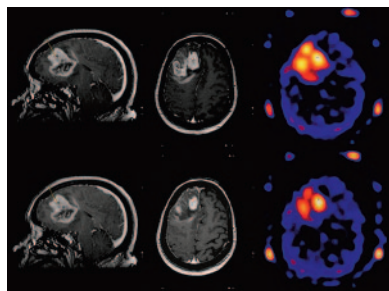
Watchman and colleagues present a radiation transport model combining chord-based techniques for tracking α -particles and a spatial model of marrow tissues to provide a basis for application of the MIRD schema to patient-specific dosimetry in new α -particle emitter therapies. . . **Page 1171**

Johnson and colleagues explore the ability of $^{99\text{m}}\text{Tc}$ -annexin SPECT to image apoptosis in the vascular wall of coronary arteries in a porcine model and discuss the clinical utility of this technique for identifying plaque apoptosis in the coronary vessels. **Page 1186**

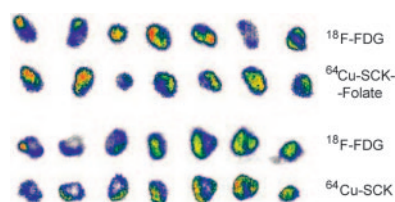
Beekman and colleagues describe a dedicated SPECT system for radionuclide imaging of murine organs at submillimeter resolutions and present in vivo images that indicate the possibilities for future highly targeted radiotracer studies in small animals. **Page 1194**



Sato and colleagues elucidate the biodistribution and tumor-targeting ability of a radiolabeled antimesothelin Fv-streptavidin fusion protein in mice and discuss the implications for clinical imaging of mesotheliomas and ovarian cancers. **Page 1201**



Watabe and colleagues report on a method for generating parametric images of myocardial blood flow, perfusable tissue fraction, and arterial blood volume with ^{15}O -water PET and discuss the utility of this method for detecting regional myocardial perfusion abnormalities. . **Page 1219**



Rossin and colleagues evaluate ^{64}Cu -radiolabeled folate-conjugated shell cross-linked nanoparticles as candidate agents to shuttle radionuclides and drugs into tumors that overexpress the folate receptor. **Page 1210**

Coleman and colleagues summarize the collaborative discussions of representatives from the American College of Radiology, the SNM, and the Society of Computed Body Tomography and Magnetic Resonance on a range of issues relating to integrated PET/CT systems in clinical settings. **Page 1225**

Koopmans and colleagues describe ^{18}F -DOPA-induced carcinoid crisis in a patient with carcinoid tumor and extensive liver metastases and advise on treatments that PET centers should have available for this rare reaction. **Page 1240**

ON THE COVER

On these images, obtained to show bone metabolism within a mouse lumbar spine, uptake in tiny parts of the individual processes is readily visualized. Also, the spaces between and within the vertebrae that do not take up tracer are clearly distinguished from bone tissue,

particularly in the isosurface renderings. Because uptake is influenced by changes in bone remodeling, such as those caused by mechanical strain or tumor growth, the type of detailed imaging shown here may initiate new research opportunities in locomotion, bone, and cancer research.

